

Generation of spin currents by the orbital Hall effect in Cu and Al and their measurement by a Ferris-wheel ferromagnetic resonance technique at the wafer level

Amit Rothschild^{1,*}, Nadav Am-Shalom^{1,*}, Nirel Bernstein^{1,*}, Ma'yan Meron^{1,*}, Tal David^{1,*}, Benjamin Assouline,¹ Elichai Frohlich,¹ Jiewen Xiao,² Binghai Yan², and Amir Capua^{1,†}

¹Department of Applied Physics, The Hebrew University of Jerusalem, Jerusalem 9190401, Israel

²Department of Condensed Matter Physics, Weizmann Institute of Science, Rehovot 7610001, Israel



(Received 6 April 2022; revised 26 September 2022; accepted 27 September 2022; published 14 October 2022)

We present a ferromagnetic resonance (FMR) method that we term the “Ferris” FMR. It is wideband, has at least an order of magnitude higher sensitivity as compared to conventional FMR systems, and measures the absorption line rather than its derivative. It is based on large-amplitude modulation of the externally applied magnetic field that effectively magnifies signatures of the spin-transfer torque making its measurement possible even at the wafer level. Using the Ferris FMR, we report the generation of spin currents from the orbital Hall effect taking place in pure Cu and Al. To this end, we use the spin-orbit coupling of a thin Pt layer introduced at the interface that converts the orbital current to a measurable spin current. While Cu reveals a large effective spin Hall angle exceeding that of Pt, Al possesses an orbital Hall effect of opposite polarity in agreement with the theoretical predictions. Our results demonstrate additional spin- and orbit functionality for two important metals in the semiconductor industry beyond their primary use as interconnects with all the advantages in power, scaling, and cost.

DOI: [10.1103/PhysRevB.106.144415](https://doi.org/10.1103/PhysRevB.106.144415)

I. INTRODUCTION

In the orbital Hall effect (OHE) a current of orbital angular momentum is generated transverse to a charge current that is passed through a metallic film in a fashion reminiscent of the spin Hall effect (SHE). It is foundational to solid-state physics and is also appealing from a technological perspective. Although the OHE was conceived [1,2] immediately after the proposal of the intrinsic SHE [3,4], its nature remained elusive because of the short orbital lifetimes. In contrast to the SHE that is often found in heavy metals such as Pt and W due to their large spin-orbit coupling (SOC) [3–6], the OHE emerges from the momentum-space orbital texture when current is passed through the crystal and does not require SOC [1,2,7–9]. Therefore, it is anticipated to be capable of generating torques more efficiently as compared to SHE but without the penalty of the large Gilbert losses [10,11]. Interestingly, the OHE was not observed until recently, e.g., in Cr [12] and Ti [13], while the orbital Rashba-Edelstein effect [14] was reported in CuO [15–18].

The conversion efficiency of charge current to spin current is known as the spin Hall angle, θ_{SH} . Reliably quantifying θ_{SH} is key to the development of spintronics technology. The ferromagnetic resonance (FMR)-based techniques [19–26] have proven pivotal for accurately determining θ_{SH} . In these measurements the generated spin-transfer torque (STT) modifies the resonance linewidth by the antidamping torque. Two common implementations of the FMR experiment are the

cavity [19,26] and stripline FMR [27,28]. While the cavity FMR benefits from high sensitivity suitable for atomically thin samples, it is narrow band. On the other hand, the stripline FMR is broadband but typically has lower sensitivity. For these reasons the spin-torque FMR (STFMR) technique [21,29–32] gained popularity for quantifying θ_{SH} in which dual AC Oersted- and spin-torque excitations produce a DC voltage that is probed electrically on a prepatterned device [33,34].

In conventional FMR techniques [19,26–28] the sensitivity is achieved by applying a small signal modulation to the external magnetic field which results in a signal of a proportionally small amplitude that represents the differential absorption. In contrast, in this work we apply a large-amplitude modulation to the externally applied magnetic field which results in an on-off modulation of the absorption, leading to a greater sensitivity to the FMR signal. Additionally, it produces a signal proportional to the actual absorption spectrum. The modulation is achieved by placing permanent magnets on a spinning disk; hence, we term the technique the *Ferris FMR*. The technique is implemented in a stripline configuration making it broadband and well suited for atomically thin films. Most importantly, the large-amplitude modulation turns out to expand the linewidth by ~ 2 –5 times. Consequently, θ_{SH} can be reliably resolved at lower applied currents and the measurement of θ_{SH} becomes possible even at the wafer scale without patterning devices. Using the Ferris FMR we demonstrate the ability to generate a sizable STT in pure Cu and Al as predicted by recent theory of the OHE [35,36]. To that end, we use the SOC of a thin layer of Pt that converts the orbital current to a spin current [12,16,36,37]. A higher effective θ_{SH} , θ_{SH}^{eff} , of the Cu-based system is found as compared to Pt while at the same

*These authors contributed equally to this work.

†amir.capua@mail.huji.ac.il

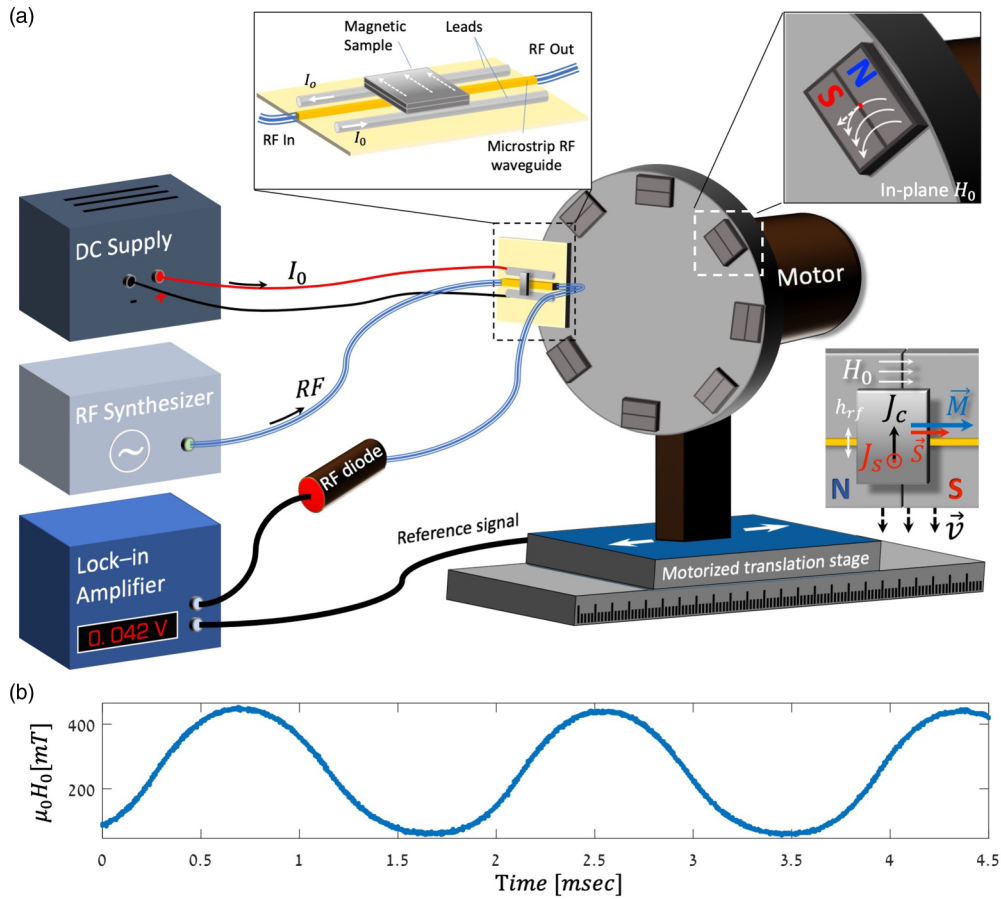


FIG. 1. (a) Ferris FMR setup. $H(t)$ is generated by rotating a magnetic disk. After passing through the waveguide, the rf signal is detected on an rf diode detector. Left inset: two flexible leads are placed on each side of the waveguide to pass current through the sample. Upper-right inset: magnified image of the magnet pairs. Lower-right inset: geometrical arrangement of the fields and currents of the experiment. h_{rf} is the rf field, \vec{v} is the magnet pair velocity, and \vec{S} is the spin orientation. (b) Measured temporal profile of $H(t)$.

time the Gilbert losses are lower. Interestingly, Al displays a negative θ_{SH}^{eff} in agreement with theoretical predictions.

II. RESULTS

The Ferris FMR setup is presented in Fig. 1(a). The magnetic film is placed on a stripline waveguide at the output of which the power of the microwave signal is monitored using an rf diode and a lock-in amplifier. The externally applied magnetic field, $H(t)$, is generated using pairs of permanent magnets of opposite polarity resulting in an in-plane field required for the measurement of θ_{SH} . A sinusoidally modulated profile of amplitude H_0 results [Fig. 1(b)] that is varied by translating the spinning disk.

The absorption spectrum is constructed in the following manner. At H_0 below the resonance field, H_{res} , the temporal absorption profile consists of a single peak per passage of the magnet pair. At $H_0 > H_{\text{res}}$, the resonance conditions are met twice per passage resulting in a double-peaked absorption profile. A numerical calculation of the temporal voltage drop profile on the rf diode, $V_{rf}(t)$, is presented in Fig. 2(a). $V_{rf}(t)$ was determined by considering a Lorentzian absorption line together with the time-varying profile of $H(t)$. Accordingly, $V_{rf}(t, H_0) = 1/(1 + \beta^2)$ with $\beta = \gamma(H(t) - H_{\text{res}})/2\pi\alpha f$, where γ , α , and f are the

gyromagnetic ratio, Gilbert damping, and rf frequency, respectively, and $H(t) = \frac{1}{2}H_0(1 + \sin\omega_{\text{mod}}t)$. ω_{mod} is the modulation frequency. H_{res} is given by Kittel's formula, $f_{\text{res}} = \gamma \frac{\mu_0}{2\pi} \cdot \sqrt{H_{\text{res}}(H_{\text{res}} + M_s)}$ where M_s is the magnetization saturation. The signal recorded on the lock-in amplifier, $V_{\text{LI}}(H_0)$, was determined by projecting $V_{rf}(t)$ on the fundamental harmonic. Figure 2(b) presents $V_{\text{LI}}(H_0)$ in addition to an ideal Lorentzian absorption line. $V_{\text{LI}}(H_0)$ is asymmetric, its peak occurring at H_{peak} , appears at a slightly higher field than H_{res} , and it is wider as compared to the ideal Lorentzian line shape. The asymmetry and the appearance of the peak at higher fields, namely, $H_{\text{peak}} > H_{\text{res}}$, stem from the fact that the resonance conditions are also met for $H_0 > H_{\text{res}}$. These effects are eliminated once a square-wave modulation profile is applied, $H(t) = \frac{1}{2}H_0(1 + \text{square}(\omega_{\text{mod}}t))$, for which case the Lorentzian absorption line is reproduced. We define the full width at half maximum (FWHM) linewidth expansion ratio by A_c . In the absence of anisotropy, we find $A_c = 2.85$, where in the general case it has to be calculated numerically as described above.

Examples of the calculated and measured asymmetric spectra for a bilayer of 7.5 Pt/7.5 Py (numbers indicate layer thicknesses in nanometers) in a die of $0.75 \times 0.5 \text{ cm}^2$ ($W \times L$) are presented in Figs. 2(c) and 2(d). The films were grown on Si/SiO₂ substrates by Ar-based DC

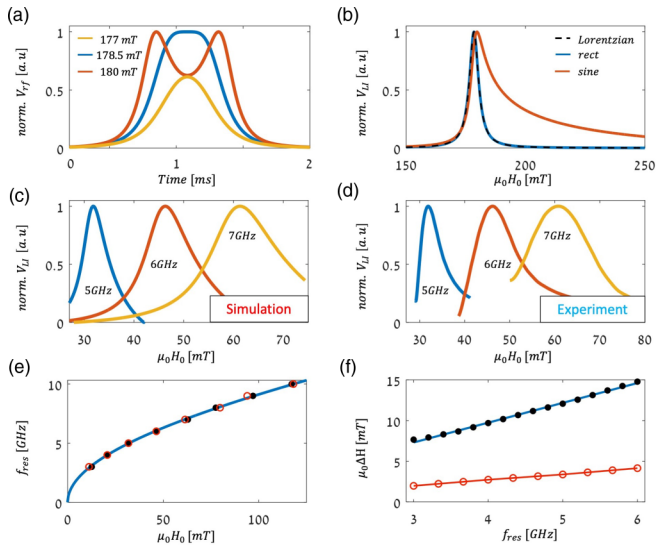


FIG. 2. (a) Calculated $V_{rf}(t)$ for $\mu_0 H_0 = 177, 178.5,$ and 180 mT corresponding to below, on, and above resonance at 5 GHz without shape anisotropy. (b) Calculation of an ideal Lorentzian absorption line (dashed black), and line shapes obtained by rectangular (solid blue) and sinusoidal modulation profiles (solid red) at 5 GHz without shape anisotropy. (c) Simulated spectra at $5, 6,$ and 7 GHz with $\alpha = 0.01$. (d) Measured spectra at $5, 6,$ and 7 GHz. (e) Measured f_{res} vs H_{peak} using Ferris FMR (black circles) and OSTFMR (open red circles). Solid line indicates fitted Kittel's formula. (f) ΔH as function of f_{res} measured by the Ferris FMR (black circles) and OSTFMR (open red circles). Blue solid line indicates linear fit.

magnetron sputtering. The base pressure before deposition was 7×10^{-10} Torr and 3×10^{-3} Torr during deposition. The base pressure was achieved by presputtering Ti for 5 min. The deposition rates for Pt, Py, and TaN were $6.55, 2.85,$ and 3.9 nm/min, respectively, achieved with power of 125 W. Using a gas mixture of nitrogen (40%) and argon (60%), 2.5 nm of TaN capping was grown. The substrates were rotated at 30 rpm and held at room temperature. In the Ferris FMR measurements, typical magnet to sample distances were $22-13$ mm while the homogeneity of $H(t)$ across the sample was verified by testing smaller $\sim 0.5 \times 0.5$ -mm² samples for which the response remained unchanged. Each magnet was 10×17 mm² placed on a disk 13 cm in diameter. The minimal incremental movement of the translation stage was 0.05 μ m so that H_0 was controllable to an accuracy of 0.6 μ T at the closer end, well beyond any requirement of an FMR experiment. $\omega_{mod}/2\pi$ was 500 Hz. f_{res} versus H_{peak} follows Kittel's formula as seen in Fig. 2(e) leading to $M_s = 7.3 \times 10^5$ A/m, which was extracted using the approximation $H_{peak} \cong H_{res}$. The results were verified using an optical STFMR (OSTFMR) experiment (open red circles) described in Ref. [38]. Figure 2(f) presents the measured FWHM linewidth, ΔH , as a function of f_{res} resulting in $\alpha = 0.0135 \pm 0.0002$ obtained using $\alpha = \gamma \Delta H / 4\pi A_c f$ and a calculated $A_c = 2.65$. OSTFMR measurements (red trace) resulted in a slightly lower value of $\alpha = 0.0124 \pm 0.0001$ where the difference may be related to the device versus film-level dynamics. As compared to the device-level

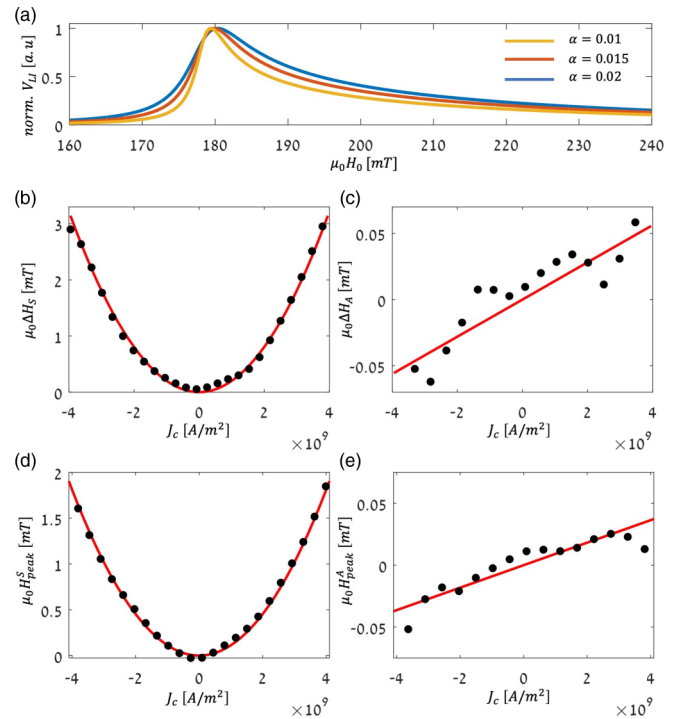


FIG. 3. SHE measurement in Pt. (a) Calculation of the Ferris FMR responses for α of 0.01 (yellow), 0.015 (red), and 0.02 (blue) at 5 GHz. (b) Measured ΔH as a function of J_c (black dots) together with ΔH_S of the fit (red solid line). (c) Antisymmetric component of (b). Red solid line is a fit of ΔH_A . (d) Measured H_{peak} as a function of J_c (black dots) and fit of H_{peak}^S (red solid line). (e) Antisymmetric component of (d).

measurement, in the wafer-level measurement an additional channel of losses exists. Magnons are emitted away from the area excited by the stripline. This channel does not exist in the device-level measurement where the magnetization precessions are driven homogeneously. Hence, the losses are lower. The detection limit of the Ferris FMR was estimated to be 1.55×10^{11} μ B from a 520×410 - μ m² sample having signal-to-noise ratio = 160.9 that is $1-2$ orders of magnitude more sensitive than conventional FMR systems [28].

To demonstrate a measurement of θ_{SH} we pass a charge current in the well-studied Pt/Py bilayer that modulates the effective α by the antidamping torque in the usual manner [21]. A calculation of the absorption spectra for three different α values is presented in Fig. 3(a) revealing that H_{peak} shifts in addition to the broadening of ΔH . The shift occurs since resonance conditions are met when $H_0 > H_{res}$. In the Pt/Py system θ_{SH}^{eff} represents the intrinsic θ_{SH} of Pt, θ_{SH}^{Pt} , normalized by the transparency of the Pt/Py interface, T_s . θ_{SH}^{Pt} accounts for the spin-diffusion length, λ_{SD} , and is layer thickness specific. The measurements here and in the ones that follow were carried out in dies of 0.75×0.5 cm² ($W \times L$). As compared to device-level measurements, achieving sufficiently high current densities, J_c , to drive a sizable SHE is more difficult due to joule heating. However, in the Ferris FMR technique the linewidth is expanded by A_c so that a measurable torque should already be obtained at A_c^{-1} of typical applied J_c . To

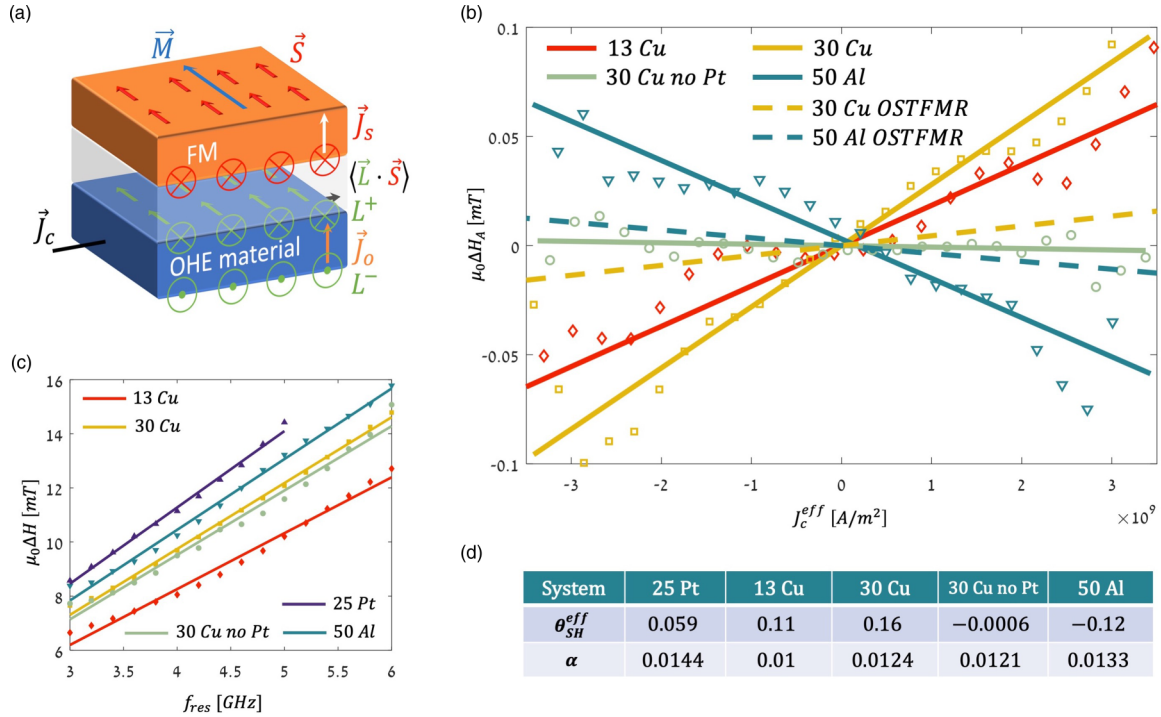


FIG. 4. OHE measurement in Cu and Al. (a) Schematic of the trilayer system. (b) Measured ΔH_A as a function of J_c^{eff} in the Cu₁₃ (red), Cu₃₀ (yellow), Cu₃₀ without Pt₁ conversion layer (light green), and Al₅₀ (dark green)-based systems at 5 GHz. Solid line represents fit to measurement. Dashed lines represent the fitted data of the OSTFMR measurements. (c) ΔH vs f_{res} . Color code same as in (b). Pt₂₅ data indicated in purple. Traces are shifted to cross origin for clarity. (d) Summary of θ_{SH} and α .

reduce the joule heating we reduce the resistance of the film by measuring a 25 Pt/5 Py bilayer that has a relatively thick Pt layer, well beyond λ_{SD} . The resistivities of the Pt and Py layers were $\rho_{Pt_{25}} = 27 \mu\Omega \text{ cm}$ and $\rho_{Py_5} = 55 \mu\Omega \text{ cm}$ (numbers in subindex indicate the thickness of the layer referred to), respectively, as determined separately for each film by Hall measurement in the van der Pauw configuration. The surface roughness of the bilayer was $R_a = 0.29 \text{ nm}$ (film roughness are indicated throughout the work as the films are introduced). J_c was driven through two semiflexible conducting leads placed to the sides of the waveguide $\sim 2 \text{ mm}$ apart [Fig. 1(a), left inset], while the resistance was monitored to assure adequate contact. The geometrical arrangement of the experiment is illustrated in the lower inset of Fig. 1(a). The measured J_c -dependent ΔH modulation is presented in Fig. 3(b) and consists of a symmetric part in J_c , ΔH_S , represented by the red solid line, and an antisymmetric part, ΔH_A , presented in Fig. 3(c). ΔH_S stems from joule heating [26] while ΔH_A stems from the generated STT. A sizable antisymmetric SHE-induced linewidth broadening is seen for $|J_c|$ of up to $4 \times 10^9 \text{ A/m}^2$, which is generally lower than typical J_c applied in θ_{SH} measurements. Following Ref. [39], we derive the relation

$$\Delta H_A \cong A_c \frac{\sqrt{H_{res}(H_{res} + M_s)}}{(1 + \alpha^2)(H_{res} + 0.5M_s)} \frac{\hbar J_s}{eM_s t_{FM}}, \quad (1)$$

where e is the electron charge, t_{FM} is the thickness of the ferromagnetic layer, and \hbar is the reduced Planck constant. $J_s = \theta_{SH}^{eff} J_c$ is the net spin-current density injected into the Py. $\alpha = 0.0144$ was determined from the Ferris FMR mea-

surement. Accordingly, $\theta_{SH, Pt}^{eff} = 0.09 \pm 0.01$ results, agreeing well with measured values for Pt [21,38–40]. Figures 3(d) and 3(e) present the measured symmetric and antisymmetric parts of the J_c -dependent H_{peak} , H_{peak}^S , and H_{peak}^A , respectively. H_{peak}^S stems from the joule heating. However, extraction of θ_{SH} from H_{peak}^A is not straightforward. From Fig. 3(a) it is seen that the influence of α on H_{peak} is significantly smaller than its effect on ΔH . In addition, H_{peak}^A is also affected by the Oersted field contribution of the Pt layer, which is antisymmetric in J_c and masks the STT contribution.

Next, we demonstrate the ability to efficiently generate STT using Cu and Al. According to OHE theory, Cu is predicted to be capable of generating significant orbital current that arises from sd hybridization resulting in sizable orbital Hall conductivity that is comparable in magnitude to the spin Hall conductivity of Pt [35,36]. In contrast to spin currents, orbital currents cannot exert a torque because of the lack of exchange coupling between orbital angular momentum and the local magnetic moment. Therefore, we introduce SOC at the Cu/Py interface by adding a thin layer of Pt that converts the orbital current into a measurable spin current [12,13,36,41]. We use the trilayer of $X_{OHE}/1 \text{ Pt}/7.5 \text{ Py}$, where $X_{OHE} = 13 \text{ Cu}$, 30 Cu , and 50 Al , as illustrated in Fig. 4(a). The high conductivity of Cu as compared to Pt enables to carry out the measurement using a thinner Cu layer. We first examine the structure of 13 Cu/1 Pt/7.5 Py ($\rho_{Py_{7.5}} = 35 \mu\Omega \text{ cm}$, $R_a = 0.31 \text{ nm}$). The Cu layer was deposited at a rate of 7 nm/min . The measured ΔH_A is summarized in Fig. 4(b) as function of an effective J_c that is the weighted current-density average passing in the spin-current

generating layers $J_c^{\text{eff}} = (J_{c,\text{Cu}}t_{\text{Cu}} + J_{c,\text{Pt}}t_{\text{Pt}})/(t_{\text{Cu}} + t_{\text{Pt}})$. A prominent modulation of ΔH_A is revealed. The measured STT stems from multiple spin and orbital-dependent processes. The orbital current generated in the Cu layer is converted at the Cu/Pt interface into spin current that follows diffusive transport into the Py and transparency at the Pt/Py interface. It is well known that the Rashba-Edelstein effect in Cu/Pt interfaces is negligible [40,42] and so is the SHE of Cu. Lastly is the contribution of the spin current generated by the SHE of Pt. Accordingly, $J_s = J_{c,\text{Cu}}T_s(\theta_{\text{SH}}^{\text{Pt}}\frac{\rho_{\text{Cu}}}{\rho_{\text{Pt}}} + \eta_{\text{LS}}\theta_{\text{OH}}^{\text{Cu}})$, where ρ_{Cu} and ρ_{Pt} are the electrical resistivities of the Cu and Pt layers, respectively. η_{LS} is the interfacial orbital-spin conversion efficiency, and $\theta_{\text{OH}}^{\text{Cu}}$ is the intrinsic orbital Hall angle of Cu. In our case $\rho_{\text{Cu}_{13}} = 21 \mu\Omega \text{ cm}$ and $\rho_{\text{Pt}_1} = 61 \mu\Omega \text{ cm}$. Namely, the maximal current density in the Pt layer is $J_{c,\text{Pt}_1} = 1.19 \times 10^9 \text{ A/m}$ and is too low to account for the observed broadening. In the trilayer, $\theta_{\text{SH}}^{\text{eff}}$ is defined by $J_s = \theta_{\text{SH}}^{\text{eff}}J_c^{\text{eff}}$. Since $J_{c,\text{Cu}_{13}}t_{\text{Cu}_{13}} \approx 39 \times J_{c,\text{Pt}_1}t_{\text{Pt}_1}$, $J_c^{\text{eff}} \cong J_{c,\text{Cu}_{13}}$ and $\theta_{\text{SH}}^{\text{eff}} \cong T_s(\theta_{\text{SH}}^{\text{Pt}}\frac{\rho_{\text{Cu}}}{\rho_{\text{Pt}}} + \eta_{\text{LS}}\theta_{\text{OH}}^{\text{Cu}})$, from which we find $\theta_{\text{SH},\text{Cu}_{13}}^{\text{eff}} = 0.110 \pm 0.012$.

Figure 4(b) also presents data for a trilayer having a thicker Cu layer of 30 Cu/1 Pt/7.5 Py ($\rho_{\text{Cu}_{30}} = 9 \mu\Omega \text{ cm}$, $R_a = 0.5 \text{ nm}$). An even larger modulation of ΔH is seen leading to $\theta_{\text{SH},\text{Cu}_{30}}^{\text{eff}} = 0.160 \pm 0.011$. The interfaces are identical to those of the Cu₁₃-based trilayer while $J_{c,\text{Pt}}$ reduces to $0.14J_{c,\text{Cu}}$ so that the contribution of the SHE within the Pt conversion layer is even further diminished. Yet, $\theta_{\text{SH},\text{Cu}_{30}}^{\text{eff}} > \theta_{\text{SH},\text{Cu}_{13}}^{\text{eff}}$, readily indicating that J_s stems from the bulk of the Cu by the generation of orbital current. Although in the previous studies of Refs. [40,42] the Cu/Pt interface did not reveal the Rashba-Edelstein effect, our observations cannot completely rule out such additional contribution. In the case of the Cu₃₀ trilayer, the term $\theta_{\text{SH}}^{\text{Pt}}\frac{\rho_{\text{Cu}_{30}}}{\rho_{\text{Pt}_1}}$ in $\theta_{\text{SH}}^{\text{eff}}$ can be neglected, and $\theta_{\text{SH}}^{\text{eff}}$ serves as a lower limit to the intrinsic $\theta_{\text{OH}}^{\text{Cu}_{30}}$, assuming a negligible Rashba-Edelstein effect.

The results were verified by conventional device-level measurements using the OSTFMR technique. The $350 \times 450\text{-}\mu\text{m}^2$ ($W \times L$) devices were fabricated from the same Cu₃₀-based film. The measurements were carried out applying higher J_c^{eff} of up to 10^{10} A/m^2 [dashed yellow line of Fig. 4(b)]. ΔH_A of the OSTFMR is narrower as expected whereas $\theta_{\text{SH},\text{Cu}_{30}}^{\text{eff}} = 0.12 \pm 0.01$, confirming the Ferris FMR measurements. However, this value is slightly lower than $\theta_{\text{SH},\text{Cu}_{30}}^{\text{eff}}$ measured by the Ferris FMR. The difference may be attributed to the joule heating and requires further investigation. In a second test, the conversion layer was removed, resulting in the bilayer of 30 Cu/7.5 Py ($R_a = 0.45 \text{ nm}$). Figure 4(b) readily shows that the modulation of ΔH_A is diminished with $\theta_{\text{SH},\text{no Pt}}^{\text{eff}} = -0.0006 \pm 0.005$.

When Cu is replaced by Al, sp orbital hybridization takes place. In this case an orbital current of opposite polarity was predicted [35]. The resistivity of Al is higher than Cu; therefore, our measurements were carried out on 50 Al/1 Pt/7.5 Py ($\rho_{\text{Al}_{50}} = 13 \mu\Omega \text{ cm}$, $R_a = 1.83 \text{ nm}$, 2.5-nm/min deposition rate of Al) and are presented in Fig. 4(b). ΔH_A reveals the predicted negative θ_{SH} [35] from which we find $\theta_{\text{SH},\text{Al}}^{\text{eff}} = -0.12 \pm 0.01$. The SHE of the Pt layer is not significant and can be neglected here as well. Even if it was not negligible, the negative $\theta_{\text{SH},\text{Al}}^{\text{eff}}$ indicates that the J_s induced

by orbital current overcomes the positive contribution of the Pt. The negative $\theta_{\text{SH},\text{Al}}^{\text{eff}}$ was also verified using the OSTFMR device-level measurement [Fig. 4(b)] leading to $\theta_{\text{SH},\text{Al}}^{\text{eff}} = -0.08 \pm 0.01$. Once more, this value is slightly lower than $\theta_{\text{SH}}^{\text{eff}}$ obtained from the Ferris FMR. A possible role of the Al/Pt interface may exist.

α critically depends on SOC by processes such as the Dyakonov-Perel and Elliot-Yafet spin relaxations. Since the OHE does not rely on SOC, it is anticipated to give rise to a high θ_{SH} with low α . In the material systems at hand, α is enhanced by spin pumping into the adjacent nonmagnetic metal [43]. Figure 4(c) presents the α measurements. Pt is well known to be an efficient sink for spin angular momentum [44,45] and indeed the largest damping is found in the 25-nm Pt-based bilayer with $\alpha_{\text{Pt}_{25}} = 0.0144 \pm 0.0003$. When the Pt layer is replaced by Cu, SOC is reduced and α decreases as seen for 30 Cu/7.5 Py, resulting in $\alpha_{\text{no Pt}} = 0.0121 \pm 0.0002$. In this case spin diffusion into the Cu takes place. Since $\lambda_{\text{SD}} \approx 450 \text{ nm}$ in Cu [46], the full thickness of the Cu layer contributes to the losses. When the 1-nm Pt conversion layer is introduced, α increases only slightly to $\alpha_{\text{Cu}_{30}} = 0.0124 \pm 0.0002$, indicating that the additional losses stemming from the conversion layer are marginal and that the primary contribution remains the bulk of the Cu. As compared to the Pt₂₅ bilayer, the Cu₃₀-based trilayer displays a higher $\theta_{\text{SH}}^{\text{eff}}$ with lower α . When the thickness of the Cu film is reduced as in the Cu₁₃ trilayer, α reduces significantly to $\alpha_{\text{Cu}_{13}} = 0.010 \pm 0.002$, providing further evidence that the losses stem from the bulk of the Cu film following spin propagation through the Pt layer. Finally, Al results in $\alpha_{\text{Al}} = 0.0133 \pm 0.003$, illustrating once more that a higher $\theta_{\text{SH}}^{\text{eff}}$ is achievable with lower α as compared to the SHE of Pt.

III. CONCLUSIONS

Al and Cu are key metals in the semiconductor industry that offer superior current-carrying capacity due to their high conductivity and excellent heat dissipation. Having overcome the fabrication challenges such as electromigration and Si contamination, they are currently considered the metals of choice for interconnects in high-volume applications which benefit from improved speed and power performance at attractively low cost. Our results demonstrate additional spin- and orbit functionality for Cu and Al beyond their use as interconnects. In agreement with OHE theory, they displayed efficient spin-current generation and low α as compared to the SHE of Pt while at the same time offering complementary spin logic. These observations were obtained in die-level measurements and are expected to facilitate the exploration of light metals for spin- and orbit-based technologies.

ACKNOWLEDGMENTS

A.C. acknowledges the support from the Israel Science Foundation (Grant No. 1217/21), the Peter Brojde Center for Innovative Engineering and Computer Science, and from the Center for Nanoscience and Nanotechnology of the Hebrew University of Jerusalem.

- [1] S. Zhang and Z. Yang, Intrinsic Spin and Orbital Angular Momentum Hall Effect, *Phys. Rev. Lett.* **94**, 066602 (2005).
- [2] B. A. Bernevig, T. L. Hughes, and S.-C. Zhang, Orbitoronics: The Intrinsic Orbital Current in p-Doped silicon, *Phys. Rev. Lett.* **95**, 066601 (2005).
- [3] S. Murakami, N. Nagaosa, and S.-C. Zhang, Dissipationless quantum spin current at room temperature, *Science* **301**, 1348 (2003).
- [4] J. Sinova, D. Culcer, Q. Niu, N. A. Sinitsyn, T. Jungwirth, and A. H. MacDonald, Universal Intrinsic Spin Hall Effect, *Phys. Rev. Lett.* **92**, 126603 (2004).
- [5] J. E. Hirsch, Spin Hall Effect, *Phys. Rev. Lett.* **83**, 1834 (1999).
- [6] Y. K. Kato, R. C. Myers, A. C. Gossard, and D. D. Awschalom, Observation of the spin hall effect in semiconductors, *Science* **306**, 1910 (2004).
- [7] H. Kontani, T. Tanaka, D. S. Hirashima, K. Yamada, and J. Inoue, Giant Intrinsic Spin and Orbital Hall Effects in Sr_2MO_4 ($M = \text{Ru}, \text{Rh}, \text{Mo}$), *Phys. Rev. Lett.* **100**, 096601 (2008).
- [8] T. Tanaka, H. Kontani, M. Naito, T. Naito, D. S. Hirashima, K. Yamada, and J. Inoue, Intrinsic spin Hall effect and orbital Hall effect in 4d and 5d transition metals, *Phys. Rev. B* **77**, 165117 (2008).
- [9] H. Kontani, T. Tanaka, D. S. Hirashima, K. Yamada, and J. Inoue, Giant Orbital Hall Effect in Transition Metals: Origin of Large Spin and Anomalous Hall Effects, *Phys. Rev. Lett.* **102**, 016601 (2009).
- [10] S. Mizukami, E. P. Sajitha, D. Watanabe, F. Wu, T. Miyazaki, H. Naganuma, M. Oogane, and Y. Ando, Gilbert damping in perpendicularly magnetized Pt/Co/Pt films investigated by all-optical pump-probe technique, *Appl. Phys. Lett.* **96**, 152502 (2010).
- [11] E. Barati, M. Cinal, D. M. Edwards, and A. Umerski, Gilbert damping in magnetic layered systems, *Phys. Rev. B* **90**, 014420 (2014).
- [12] S. Lee, M.-G. Kang, D. Go, D. Kim, J.-H. Kang, T. Lee, G.-H. Lee, J. Kang, N. J. Lee, Y. Mokrousov, S. Kim, K.-J. Kim, K.-J. Lee, and B.-G. Park, Efficient conversion of orbital Hall current to spin current for spin-orbit torque switching, *Commun. Phys.* **4**, 234 (2021).
- [13] Y.-G. Choi, D. Jo, K.-H. Ko, D. Go, K.-H. Kim, H. Gyum Park, C. Kim, B.-C. Min, G.-M. Choi, and H.-W. Lee, [arXiv:2109.14847](https://arxiv.org/abs/2109.14847) (2021).
- [14] D. Go, D. Jo, T. Gao, K. Ando, S. Blügel, H.-W. Lee, and Y. Mokrousov, Orbital Rashba effect in a surface-oxidized Cu film, *Phys. Rev. B* **103**, L121113 (2021).
- [15] H. An, Y. Kageyama, Y. Kanno, N. Enishi, and K. Ando, Spin-torque generator engineered by natural oxidation of Cu, *Nat. Commun.* **7**, 13069 (2016).
- [16] S. Ding, A. Ross, D. Go, L. Baldrati, Z. Ren, F. Freimuth, S. Becker, F. Kammerbauer, J. Yang, G. Jakob, Y. Mokrousov, and M. Kläui, Harnessing Orbital-to-Spin Conversion of Interfacial Orbital Currents for Efficient Spin-Orbit Torques, *Phys. Rev. Lett.* **125**, 177201 (2020).
- [17] Y. Tazaki, Y. Kageyama, H. Hayashi, T. Harumoto, T. Gao, J. Shi, and K. Ando, Current-induced torque originating from orbital current, [arXiv:2004.09165](https://arxiv.org/abs/2004.09165) (2020).
- [18] S. Ding, Z. Liang, D. Go, C. Yun, M. Xue, Z. Liu, S. Becker, W. Yang, H. Du, C. Wang, Y. Yang, G. Jakob, M. Kläui, Y. Mokrousov, and J. Yang, Observation of the Orbital Rashba-Edelstein Magnetoresistance, *Phys. Rev. Lett.* **128**, 067201 (2022).
- [19] K. Ando, S. Takahashi, K. Harii, K. Sasage, J. Ieda, S. Maekawa, and E. Saitoh, Electric Manipulation of Spin Relaxation Using the Spin Hall Effect, *Phys. Rev. Lett.* **101**, 036601 (2008).
- [20] O. Mosendz, V. Vlaminck, J. E. Pearson, F. Y. Fradin, G. E. W. Bauer, S. D. Bader, and A. Hoffmann, Detection and quantification of inverse spin Hall effect from spin pumping in permalloy/normal metal bilayers, *Phys. Rev. B* **82**, 214403 (2010).
- [21] L. Liu, T. Moriyama, D. C. Ralph, and R. A. Buhrman, Spin-Torque Ferromagnetic Resonance Induced by the Spin Hall Effect, *Phys. Rev. Lett.* **106**, 036601 (2011).
- [22] F. D. Czeschka, L. Dreher, M. S. Brandt, M. Weiler, M. Althammer, I. M. Imort, G. Reiss, A. Thomas, W. Schoch, W. Limmer, H. Huebl, R. Gross, and S. T. B. Goennenwein, Scaling Behavior of the Spin Pumping Effect in Ferromagnet-Platinum Bilayers, *Phys. Rev. Lett.* **107**, 046601 (2011).
- [23] V. Vlaminck, J. E. Pearson, S. D. Bader, and A. Hoffmann, Dependence of spin-pumping spin Hall effect measurements on layer thicknesses and stacking order, *Phys. Rev. B* **88**, 064414 (2013).
- [24] L. Bai, P. Hyde, Y. S. Gui, C. M. Hu, V. Vlaminck, J. E. Pearson, S. D. Bader, and A. Hoffmann, Universal Method for Separating Spin Pumping from Spin Rectification Voltage of Ferromagnetic Resonance, *Phys. Rev. Lett.* **111**, 217602 (2013).
- [25] D. Wei, M. Obstbaum, M. Ribow, C. H. Back, and G. Woltersdorf, Spin Hall voltages from a.c. and d.c. spin currents, *Nat. Commun.* **5**, 3768 (2014).
- [26] S. Emori, T. Nan, T. M. Oxholm, C. T. Boone, J. G. Jones, B. M. Howe, G. J. Brown, D. E. Budil, and N. X. Sun, Quantification of the spin-Hall anti-damping torque with a resonance spectrometer, *Appl. Phys. Lett.* **106**, 022406 (2015).
- [27] S. S. Kalarickal, P. Krivosik, M. Wu, C. E. Patton, M. L. Schneider, P. Kabos, T. J. Silva, and J. P. Nibarger, Ferromagnetic resonance linewidth in metallic thin films: Comparison of measurement methods, *J. Appl. Phys.* **99**, 093909 (2006).
- [28] I. Neudecker, G. Woltersdorf, B. Heinrich, T. Okuno, G. Gubbiotti, and C. H. Back, Comparison of frequency, field, and time domain ferromagnetic resonance methods, *J. Magn. Magn. Mater.* **307**, 148 (2006).
- [29] A. Azevedo, L. H. Vilela-Leão, R. L. Rodríguez-Suárez, A. F. Lacerda Santos, and S. M. Rezende, Spin pumping and anisotropic magnetoresistance voltages in magnetic bilayers: Theory and experiment, *Phys. Rev. B* **83**, 144402 (2011).
- [30] K. Kondou, H. Sukegawa, S. Mitani, K. Tsukagoshi, and S. Kasai, Evaluation of spin Hall angle and spin diffusion length by using spin current-induced ferromagnetic resonance, *Appl. Phys. Express* **5**, 073002 (2012).
- [31] K.-U. Demasius, T. Phung, W. Zhang, B. P. Hughes, S.-H. Yang, A. Kellock, W. Han, A. Pushp, and S. S. P. Parkin, Enhanced spin-orbit torques by oxygen incorporation in tungsten films, *Nat. Commun.* **7**, 10644 (2016).
- [32] K. Kondou, H. Sukegawa, S. Kasai, S. Mitani, Y. Niimi, and Y. Otani, Influence of inverse spin Hall effect in spin-torque ferromagnetic resonance measurements, *Appl. Phys. Express* **9**, 023002 (2016).

- [33] Y. Zhang, Q. Liu, B. F. Miao, H. F. Ding, and X. R. Wang, Anatomy of electrical signals and dc-voltage line shape in spin-torque ferromagnetic resonance, *Phys. Rev. B* **99**, 064424 (2019).
- [34] R. Ben-Shalom, N. Bernstein, S. S. P. Parkin, S.-H. Yang, and A. Capua, Determination of the spin Hall angle by the inverse spin Hall effect, device level ferromagnetic resonance, and spin torque ferromagnetic resonance: A comparison of methods, *Appl. Phys. Lett.* **119**, 042401 (2021).
- [35] D. Jo, D. Go, and H.-W. Lee, Gigantic intrinsic orbital Hall effects in weakly spin-orbit coupled metals, *Phys. Rev. B* **98**, 214405 (2018).
- [36] J. Xiao, Y. Liu, and B. Yan, in *Memorial Volume for Shoucheng Zhang* (World Scientific, Singapore, 2020), pp. 353.
- [37] Y. Liu, J. Xiao, J. Koo, and B. Yan, Chirality-driven topological electronic structure of DNA-like materials, *Nat. Mater.* **20**, 638 (2021).
- [38] B. Grover, B. K. Hazra, T. Ma, B. Pal, N. Bernstein, A. Rothschild, A. K. Srivastava, S. Choudhury, G. Woltersdorf, A. Capua, and S. S. P. Parkin, Crystallographic dependence of the spin Hall angle in epitaxial Pt films: comparison of optical and electrical detection of spin-torque ferromagnetic resonance techniques, *Appl. Phys. Lett.* **120**, 172406 (2022).
- [39] A. Capua, T. Wang, S.-H. Yang, C. Rettner, T. Phung, and S. S. P. Parkin, Phase-resolved detection of the spin Hall angle by optical ferromagnetic resonance in perpendicularly magnetized thin films, *Phys. Rev. B* **95**, 064401 (2017).
- [40] W. Zhang, W. Han, X. Jiang, S.-H. Yang, and S. S. P. Parkin, Role of transparency of platinum-ferromagnet interfaces in determining the intrinsic magnitude of the spin Hall effect, *Nat. Phys.* **11**, 496 (2015).
- [41] D. Go and H.-W. Lee, Orbital torque: torque generation by orbital current injection, *Phys. Rev. Res.* **2**, 013177 (2020).
- [42] T. Nan, S. Emori, C. T. Boone, X. Wang, T. M. Oxholm, J. G. Jones, B. M. Howe, G. J. Brown, and N. X. Sun, Comparison of spin-orbit torques and spin pumping across NiFe/Pt and NiFe/Cu/Pt interfaces, *Phys. Rev. B* **91**, 214416 (2015).
- [43] C. Swindells and D. Atkinson, Interface enhanced precessional damping in spintronic multilayers: A perspective, *J. Appl. Phys.* **131**, 170902 (2022).
- [44] Y. Tserkovnyak, A. Brataas, and G. E. W. Bauer, Enhanced Gilbert Damping in Thin Ferromagnetic Films, *Phys. Rev. Lett.* **88**, 117601 (2002).
- [45] M. Caminale, A. Ghosh, S. Auffret, U. Ebels, K. Ollefs, F. Wilhelm, A. Rogalev, and W. E. Bailey, Spin pumping damping and magnetic proximity effect in Pd and Pt spin-sink layers, *Phys. Rev. B* **94**, 014414 (2016).
- [46] S. Yakata, Y. Ando, T. Miyazaki, and S. Mizukami, Temperature dependences of spin-diffusion lengths of Cu and Ru layers, *Jpn. J. Appl. Phys.* **45**, 3892 (2006).